



# Photocatalytic production of hydrogen from methanol and saccharides using carbon nanotube-TiO<sub>2</sub> catalysts

Cláudia G. Silva<sup>a,\*</sup>, Maria J. Sampaio<sup>a</sup>, Rita R.N. Marques<sup>a</sup>, Liliana A. Ferreira<sup>a</sup>, Pedro B. Tavares<sup>b</sup>, Adrián M.T. Silva<sup>a</sup>, Joaquim L. Faria<sup>a</sup>

<sup>a</sup> LCM - Laboratório de Catálise e Materiais - Laboratório Associado LSRE-LCM, Faculdade de Engenharia, Universidade do Porto, Rua Dr. Roberto Frias s/n 4200-465 Porto, Portugal

<sup>b</sup> Universidade de Trás-os-Montes e Alto Douro, Centro de Química-Vila Real, Departamento de Química, 5001-911 Vila Real, Portugal

## ARTICLE INFO

### Article history:

Received 22 July 2014

Received in revised form 6 October 2014

Accepted 10 October 2014

Available online 22 October 2014

### Keywords:

Photocatalysis

Hydrogen

Carbon nanotubes

Titanium dioxide

Saccharides

## ABSTRACT

Carbon nanotube-titanium dioxide composite materials were produced by two routes: hydration–dehydration and one-pot oxidation. Au, Pt, Ir and Pd were loaded on TiO<sub>2</sub>-based materials by an incipient wetness method. The resulting materials were calcined and afterwards reduced at two distinct temperatures, 473 and 673 K. Characterization was carried out by temperature programmed desorption, infrared and UV–Vis spectroscopy, N<sub>2</sub> adsorption, SEM and TEM. Compared with reference TiO<sub>2</sub>, composite catalysts presented increased activity for photocatalytic production of H<sub>2</sub> from methanol solutions. The highest activity was obtained for the Pt-loaded composite produced by the one-pot synthesis method, with 485 μmol of H<sub>2</sub> being generated after two hours of irradiation, contrasting with 205 μmol of H<sub>2</sub> obtained using Pt/TiO<sub>2</sub>. This synergic effect was discussed in terms of the action of carbon nanotubes as dispersing media for TiO<sub>2</sub> particles as well as their action as photosensitizers. The relative efficiency of the catalysts was related to the work function of each metal and the sizes of the metal nanoparticles. H<sub>2</sub> generation from photocatalytic reforming of saccharides, namely arabinose, glucose, fructose and cellobiose was performed using TiO<sub>2</sub> and CNT-TiO<sub>2</sub> based catalysts. The relative efficiency of H<sub>2</sub> production from these biomass-derived compounds has been discussed based on their structural arrangement, H:C ratio and availability of α-hydrogens.

© 2014 Elsevier B.V. All rights reserved.

## 1. Introduction

Energy and economy are two indissociable concepts in today's agendas of the global leaders, opinion makers, and stakeholders. A hydrogen-based economy started to fill the government programs in the beginning of the XXI century and still stores for a large share of their budgets. Hydrogen (H<sub>2</sub>) has been seen as the fuel of the future due to its bountiful abundance all over the planet and its non-polluting energetic conversion. However, while H<sub>2</sub> is widely considered as an attractive energy source to replace conventional fossil fuels, both from the environmental and economic standpoints, many practical aspects need to be solved before it can power the engines of our automobiles, or be delivered to our homes. The sustainable production of such non-polluting fuel by the conversion of natural renewable resources like solar energy into chemical energy constitutes an enormous challenge in the present.

The main route for H<sub>2</sub> production is by reforming, or partial oxidation of hydrocarbons [1,2]. The greatest drawback of these methods is the production of CO<sub>2</sub> and the great amounts of energy required. Biomass is already an important source of H<sub>2</sub> [3–5]. Hydrogen is mainly produced by biomass gasification, but this process is limited to specific applications using midsize-scale facilities, due to the costs of operation [5]. Water electrolysis is a well proven technology, which is appointed as the choice of the future for H<sub>2</sub> production, basically because relies on an inexhaustible source, such as water. However it is intensive on energy use and the production of the electricity needed for the process is an issue needing solution [6].

Looking at the above three angles, reforming, biomass and electrolysis, by the converging lenses of photolysis, in the neat sense of photon induced processes, is a significant step towards sustainable production of non-polluting fuels by converting natural renewable resources into chemical energy. Photocatalytic water splitting [7] and photocatalytic reforming of biomass [8] are two promising methods for the sustainable production of H<sub>2</sub>. The second process, in particular, combines simultaneous H<sub>2</sub> production

\* Corresponding author. Tel.: +351 225 081 779; fax: +351 225 081 449.  
E-mail addresses: [cgsilva@fe.up.pt](mailto:cgsilva@fe.up.pt) (C.G. Silva), [jlfaria@fe.up.pt](mailto:jlfaria@fe.up.pt) (J.L. Faria).

and biomass oxidation [9–11]. The major advantage is that  $H_2$  can be efficiently produced by photocatalytic degradation of organic compounds present in aqueous media at mild conditions, with simultaneous treatment/valorization of industrial wastes or by-products. This method becomes even more attractive if solar energy can be used as light source, being a relevant aspect especially in countries with high insolation levels, which is the case of southern European countries. The overall benefit is the generation of a clean, storable and renewable fuel ( $H_2$ ) with simultaneous treatment and valorization of biomass-containing streams using an inexhaustible natural resource (the Sun) as light source.

Most of the existing photo-assisted technologies are based on titanium dioxide ( $TiO_2$ ). However, a major limitation of this material is the lack of response to visible radiation, as it requires UV light photoactivation, which only accounts for 5% of the incoming solar energy. Carbon materials, in particular carbon nanotubes (CNT), have proved to produce beneficial effects on the photocatalytic activity of  $TiO_2$ , in applications ranging from wastewater treatment to  $H_2$  production, by inducing synergies between the metal oxide and the carbon phase [12–15]. Ahmad et al. have reported the use of single-walled carbon nanotubes (SWCNT)/ $TiO_2$  mechanical mixtures for  $H_2$  production from water/alcohol solutions under UV irradiation [16]. A synergy effect was observed, which was attributed to the action of SWCNT as sinks for the electrons photogenerated upon  $TiO_2$  excitation. Multi-walled carbon nanotube (MWCNT)- $TiO_2$  composites loaded with Pt nanoparticles have been used for the photocatalytic  $H_2$  generation from triethanolamine solutions under both UV and visible-light irradiation [17,18]. While bare  $TiO_2$  and MWCNT alone didn't show any catalytic activity, MWCNT- $TiO_2$  composites promoted the photocatalytic production of  $H_2$  under visible light conditions, which was ascribed to an increase in light absorption and charge separation in the composite material. CNT were also combined with other semiconductors, namely CdS [19] and CdSe [20], to improve  $H_2$  generation.

Carbohydrates, including mono-, di-, and poly-saccharides, have been used as sacrificial electron donors for the photocatalytic generation of  $H_2$  in the presence of  $TiO_2$  catalysts loaded with noble metals [21,22]. Yet no reference to the use of CNT- $TiO_2$  composites for the photocatalytic reforming of such biomass-derived compounds could be found in the literature.

In the present work CNT- $TiO_2$  composite materials are synthesized and tested for the photocatalytic production of  $H_2$  from biomass-containing aqueous solutions, namely from methanol and saccharides. The efficiency of  $H_2$  photocatalytic generation from water/methanol mixtures has been assessed in terms of CNT- $TiO_2$  photocatalyst production route and metal (Pt, Pd, Au and Ir) loading conditions. A comparative study on the use of  $TiO_2$  and CNT- $TiO_2$  catalysts for  $H_2$  production from saccharide (glucose, fructose, arabinose and cellobiose) solutions has been performed.

## 2. Experimental

### 2.1. Materials and chemicals

Multi-walled CNT synthesized by chemical vapor deposition (CVD) were purchased from Shenzhen Nanotechnologies Co. Ltd. (manufacturer data: purity  $\geq 95\%$ , main range of diameter  $< 10$  nm, length = 5–15  $\mu m$ , ash content  $\leq 0.2$  wt.%, amorphous carbon  $< 3\%$ ). The presence of trace amounts of Co, Cu and Mo catalyst residues on pristine CNT was detected by EDXS. Titanium (IV) oxide powder anatase, 99.8% metal basis was purchased from Sigma-Aldrich.

Metal salt precursors namely palladium (II) chloride ( $PdCl_2$ ), hydrogen tetrachloroaurate (III) trihydrate ( $HAuCl_4 \cdot 3H_2O$ ), dihydrogen hexachloroiridate (IV) hydrate ( $H_2IrCl_6 \cdot xH_2O$ )

and dihydrogen hexachloro palatinate (IV) hexahydrate ( $H_2PtCl_6 \cdot 6H_2O$ ) were supplied by Alfa Aesar. Nitric acid (65 wt.%  $HNO_3$ ) and glucose (D-(+)-glucose,  $C_6H_{12}O_6$ , 99.5%), were obtained from Fluka and Sigma-Aldrich, respectively. Arabinose (D-(–)-arabinose,  $C_5H_{10}O_5$ , 99+ %), fructose (D-(–)-fructose,  $C_6H_{12}O_6$ , 99%) and cellobiose (D-(+)-cellobiose,  $C_{12}H_{22}O_{11}$ , 98%) were purchased from Acros Organics.

### 2.2. Catalysts synthesis

Removal of catalytic metal residues and functionalization of the carbon nanotubes was accomplished by immersing 0.5 g of pristine CNT in 150 mL of 10 M nitric acid solution [23,24]. The suspension was heated to boiling temperature and kept under magnetic stirring for 3 h in a round bottom flask equipped with a condenser. After cooling, the suspension was washed several times with distilled water, until neutrality of the rinsing waters. The recovered powders were dried overnight at 383 K and labeled as CNTox.

The CNTox- $TiO_2$  composite was prepared by a hydration–dehydration procedure [25]: 0.1 g of functionalized CNT and 0.5 g of  $TiO_2$  were dispersed in 1 L of distilled water under magnetic stirring. The mixture was heated up to 353 K to evaporate most of the water. Then the composites were dried overnight at 383 K to eliminate the remaining humidity.

For the synthesis of (CNT- $TiO_2$ )ox, the same experimental procedure as described for the functionalization of CNT was used, but in this case both CNT and  $TiO_2$  were added simultaneously (one-pot) into the  $HNO_3$  solution.

The metal phase was loaded by incipient wetness impregnation, from the aqueous solutions of the corresponding metal salts [26]. The metal content was fixed at 1 wt.%. After impregnation, the samples were dried at 373 K for 24 h. The catalysts were heat treated under nitrogen flow for 1 h and reduced under hydrogen for 3 h at 473 K or 673 K. The temperatures were selected based on preliminary TPR analysis of given metal loaded  $TiO_2$  materials (see Supplementary Information, Fig. S11), which revealed that Pt and Pd are reduced at temperatures between 373 and 473 K, while Ir and Au show broader reduction peaks up to 673 K. In addition, the TPR profiles obtained for (CNT- $TiO_2$ )ox based materials show some differences when compared to those of  $TiO_2$  (not shown). In general, reduction peaks are broader, which indicate the existence of different interactions between the metal precursors and (CNT- $TiO_2$ )ox. Since in all cases reduction of the metals occurs up to 473 or 673 K it was decided to calcine/reduce the  $TiO_2$  and (CNT- $TiO_2$ )ox materials loaded with the different metals at those limit temperatures.

Materials were coded according to a M/S-T scheme, where “M” corresponds to the metal (Pt, Pd, Ir or Au), “S” to the semiconductor phase ( $TiO_2$ , CNTox- $TiO_2$  or (CNT- $TiO_2$ )ox) and “T” to the temperature of calcination/reduction in Kelvin (473 or 673).

### 2.3. Catalysts characterization

The morphology of the powder materials was analyzed by using scanning electron microscopy (SEM) in a FEI Quanta 400FEG ESEM instrument. Elemental analysis of the prepared catalysts was performed by energy-dispersive X-ray spectroscopy (EDXS) in an EDAX Genesis X4 M instrument. Transmission electron microscopy (TEM) was performed in a LEO 906E instrument operating at 120 kV, equipped with a 4 Mpixel  $28 \times 28$  mm CCD camera from TRS. A minimum of 60 counts was performed for the determination of the metal particle average size.

X-ray diffraction (XRD) analysis was carried out in a PANalytical X'Pert MPD equipped with a X'Celerator detector and secondary monochromator ( $Cu K\alpha \lambda = 0.154$  nm, 40 kV, 30 mA; data recorded at a 0.017 step size, 100 s/step). Rietveld refinement with PowderCell software was used to identify the crystallographic

phases present and to calculate the crystallite size from the XRD diffraction patterns.

The textural characterization of the materials was based on the corresponding  $N_2$  adsorption–desorption isotherms at 77 K, measured on a Quantachrome NOVA 4200e apparatus. All samples were first degassed in vacuum for 3 h at 393 K before analysis. The BET specific surface area ( $S_{BET}$ ) was determined from the nitrogen adsorption data within the 0.05–0.15 range of relative pressure.

Temperature programmed desorption (TPD) analysis was carried out using an AMI-300 instrument (Altamira Instruments) equipped with a quadrupole mass spectrometer (Ametek, Mod. Dymaxion). The sample (0.1 g) was placed in a U-shaped quartz tube and heated at  $5\text{ K min}^{-1}$  until the maximum temperature of 1273 K, under a constant flow of  $25\text{ cm}^3\text{ (STP) min}^{-1}$  of helium, used as carrier gas. Temperature programmed reduction (TPR) experiments were carried out in the same apparatus. In this case, the sample (150 mg) was heated at  $5\text{ K min}^{-1}$  up to the desired temperature under a flow of 5% (v/v)  $H_2$  diluted in He (total flow rate of  $30\text{ cm}^3\text{ (STP) min}^{-1}$ ). The  $H_2$  consumption was followed by using a thermal conductivity detector (TCD).

UV–Vis diffuse reflectance spectra (220–800 nm) of the powder samples were recorded on a JASCO V-560 UV–Vis spectrophotometer, with a double monochromator, double beam optical system. The spectrophotometer was equipped with an integrating sphere attachment (JASCO ISV-469). The reflectance spectra were converted by the instrument software (JASCO) to the equivalent absorption Kubelka–Munk units.

Fourier transform infrared (FTIR) measurements were performed on a FTIR Nicolet 510-P spectrometer (Thermo Fisher Scientific, USA) equipped with a MIRacle™ Single Reflection ATR (attenuated total reflectance ZnSe crystal plate) accessory (PIKE Technologies, USA).

#### 2.4. Photocatalytic reactions

The photocatalytic runs were carried out in a cylindrical glass immersion photo-reactor equipped with a Heraeus TQ 150 medium pressure mercury vapor lamp ( $\lambda_{exc} = 254, 313, 365, 436$  and  $546\text{ nm}$ ) located axially in the reactor and held in a quartz immersion tube. A DURAN® glass cooling jacket was used for irradiation in the near-UV to visible light range ( $\lambda_{exc} \geq 365\text{ nm}$ , see Supplementary Information, Fig. SI2). During the photocatalytic experiments, the temperature was kept at around 298 K. The reactor was charged with 170 mL of the aqueous solution, either 10 vol.% (2.5 M) in methanol (Fisher Scientific, 99.99%) or 0.02 M in saccharide, and containing 170 mg of catalyst (catalyst load of  $1\text{ g L}^{-1}$ ). The suspension was first degassed by a nitrogen flow for 20 min, after which the light was turned on. During measurements, the  $N_2$  flow was maintained at  $10\text{ cm}^3\text{ min}^{-1}$ . Hydrogen was detected on-line by using an Inficon Micro GC 3000 gas chromatograph equipped with a molsieve column and a micro-TCD detector, using argon as carrier gas. All the photocatalytic experiments were replicated 3 times. The reported data corresponds to the average over 3 independent runs. The standard deviation was never higher than 5%.

Four saccharide molecules were used as biomass model compounds: arabinose, fructose, cellobiose and glucose. The analysis of the saccharide solutions after 2 h of irradiation was carried out by high-performance liquid chromatography (HPLC). The chromatograph (Elite LaChrom HITACHI) was equipped with a refractive index and ultraviolet (set to 210 nm) detectors. Reactant and products were separated in an ion exclusion column (Alltech OA 1000). The eluent solution consisted of 0.05 M  $H_2SO_4$ . A volume of 50  $\mu\text{L}$  was injected and measured over 20 min, with a constant flow of  $0.5\text{ mL min}^{-1}$ .

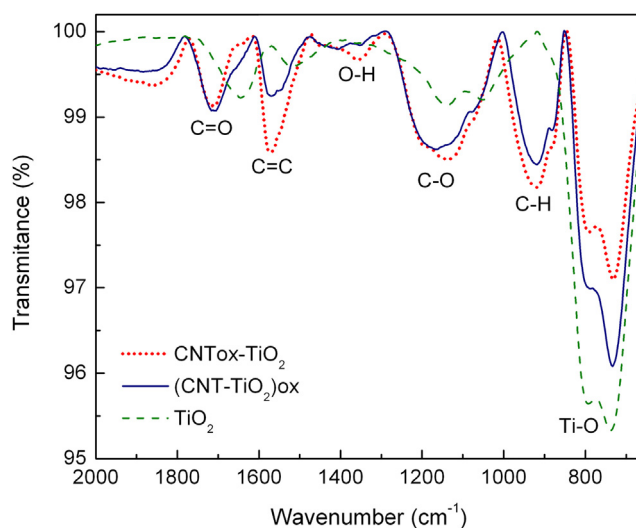


Fig. 1. Infrared ATR spectra of bare  $TiO_2$ ,  $CNT_{ox}-TiO_2$  and  $(CNT-TiO_2)_{ox}$  composites.

### 3. Results and discussion

#### 3.1. Catalysts characterization

The surface chemistry of the oxidized CNT was characterized by TPD analysis (see Supplementary Information, Fig. SI2). Oxygen surface groups on carbon materials are thermally decomposed into CO and  $CO_2$  at given temperatures, corresponding to particular functional groups [27,28] that can be quantified from the areas in the TPD spectra. Carboxylic acids are decomposed into  $CO_2$  at low temperatures ( $\sim 500$ – $550\text{ K}$ ), while lactones are released as  $CO_2$  at higher temperatures ( $880$ – $980\text{ K}$ ). Phenols and carbonyl/quinone groups decompose into CO at high temperatures ( $\sim 900$ – $950\text{ K}$  and  $\sim 1060$ – $1300\text{ K}$ , respectively). Finally, some groups such as anhydrides are released as both CO and  $CO_2$  at intermediate temperatures ( $\sim 600$ – $790\text{ K}$ ). The amounts of the individual surface groups were estimated by deconvolution of the TPD spectra using a multiple Gaussian function [27]. The main groups released from  $CNT_{ox}$  surface were phenols (57%), carboxylic acids (22%), followed by anhydrides (10%), carbonyl/quinones (9%) and finally lactones (2%).

Vibrational (FTIR) spectra of bare  $TiO_2$ ,  $CNT_{ox}-TiO_2$  and  $(CNT-TiO_2)_{ox}$  composites are displayed in Fig. 1. A strong band between 650 and  $850\text{ cm}^{-1}$ , typical from Ti–O vibration is common to all spectra. Typical bands of oxygen containing surface groups could be identified in the spectra of  $CNT_{ox}$  and of both composites [29,30]: (i) a band at around  $900\text{ cm}^{-1}$ , ascribed to isolated aromatic C–H out-of-plane bending mode vibration; (ii) a peak at  $1190\text{ cm}^{-1}$  corresponding to the C–O stretching vibration in ethers and phenols; (iii) a band peaking at  $1400\text{ cm}^{-1}$  attributed to O–H bending in phenols and carbonyls; (iv) a peak at  $1580\text{ cm}^{-1}$  assigned to aromatic ring vibration; and (v) a band at  $1715\text{ cm}^{-1}$  assigned to the C=O stretching vibration in lactones, carboxylic acids, and anhydrides.

In the case of  $(CNT-TiO_2)_{ox}$  a decrease in the intensity of the bands corresponding to O–H and C–O when compared to the spectra of  $CNT_{ox}-TiO_2$  suggests that  $TiO_2$  may be attached to CNT surface groups such as phenols and carboxylic acids. Also, the bands originated from C=C and C–H, due to aromatic ring vibrations, are less intense in  $(CNT-TiO_2)_{ox}$  than in  $CNT_{ox}-TiO_2$ , which indicates a better dispersion of the  $TiO_2$  particles at the surface of CNT in the former composite. This observation is in line with the higher intensity of the Ti–O band in the  $(CNT-TiO_2)_{ox}$  composite, revealing that the  $TiO_2$  particles are better distributed over the surface of CNT.

**Table 1**

Surface area ( $S_{\text{BET}}$ ) of pristine and oxidized carbon nanotubes, bare  $\text{TiO}_2$  and CNT- $\text{TiO}_2$  hybrid materials, and rate of  $\text{H}_2$  generation ( $r$  and  $r/S_{\text{BET}}$ ) from water/methanol solutions using the respective Pt/S-473 catalysts.

Material	$S_{\text{BET}}$ ( $\text{m}^2 \text{g}^{-1}$ )	$r$ ( $\mu\text{mol min}^{-1} \text{g}_{\text{cat}}^{-1}$ )	$r/S_{\text{BET}}$ ( $\mu\text{mol min}^{-1} \text{m}^{-2}$ )
CNT	94	–	–
CNTox	155	–	–
$\text{TiO}_2$	11	9.8	0.891
CNTox- $\text{TiO}_2$	55	15	0.271
(CNT- $\text{TiO}_2$ )ox	61	23	0.379

The surface areas of bare  $\text{TiO}_2$  and CNT, CNTox and composite materials, calculated by the BET method ( $S_{\text{BET}}$ ) are listed in Table 1. The liquid-phase oxidation treatment applied to pristine CNT led to an increase in the surface area of the resulting material. The  $S_{\text{BET}}$  of CNTox is 67% higher than that of the original material. This occurs because the severe treatment with  $\text{HNO}_3$  generates sidewall defects and opens up the end caps of the CNT [31]. The introduction of CNT led to an increase in the surface area of the resulting composites when compared to  $\text{TiO}_2$ . Worth mentioning is that the surface area of both composites is higher than the theoretical value ( $35 \text{ m}^2 \text{g}^{-1}$ ), obtained as the weighted average of the  $S_{\text{BET}}$  of CNTox and  $\text{TiO}_2$  phases in the composite materials taking into account its relative weight fraction (c.a. 17 wt.% of carbon phase, as confirmed by thermogravimetric analysis). These results suggest that the oxidative treatment promotes  $\text{TiO}_2$  particle dispersion avoiding agglomeration, thus increasing the surface area of the resulting materials. In the case of (CNT- $\text{TiO}_2$ )ox, this effect was even more pronounced, which must be related to a better distribution of the  $\text{TiO}_2$  particles in the composite catalyst due to the simultaneous CNT oxidation and formation of the composite material. It was confirmed that metal loading did not produce any significant change in the surface area of the different materials.

By SEM the typical morphology of  $\text{TiO}_2$  was observed consisting of spheroidal particles with dimensions of hundreds of nanometers (Fig. 2a), as further confirmed by TEM analysis (Fig. 2c). In the case of the composite materials, the carbon nanotubes are uniformly distributed into the  $\text{TiO}_2$  matrix, as illustrated in Fig. 2b for (CNT- $\text{TiO}_2$ )ox. The TEM analysis of this material revealed the existence of a good contact between the  $\text{TiO}_2$  and CNT phases (Fig. 2d).

In the case of metal loaded- $\text{TiO}_2$ , the TEM images revealed in most of the cases a good dispersion of the metal nanoparticles over the  $\text{TiO}_2$  phase, as can be observed for Pt/ $\text{TiO}_2$ -473 in Fig. 2e. That material shows spheroidal Pt particles of very low dimension, ranging between 1 and 5 nm (average particle size of 2.6 nm). The sizes of the metal particles depended on the type of metal and on the thermal treatment temperature, bigger particles being generally observed for the materials calcined and reduced at 673 K due to sintering phenomena (Table 2). In the case of the CNT- $\text{TiO}_2$  materials, TEM images confirmed the existence of metal nanoparticles

**Table 2**

Rate of  $\text{H}_2$  evolution ( $r$ ) from water/methanol solution using metal-loaded  $\text{TiO}_2$  and (CNT- $\text{TiO}_2$ )ox catalysts reduced at different temperatures (473 or 673 K) and average dimensions of the metal nanoparticles ( $d_{\text{M}}$ ), determined by TEM analysis.

Cocatalyst	$r$ ( $\mu\text{mol min}^{-1} \text{g}_{\text{cat}}^{-1}$ )				$d_{\text{M}}$ (nm) <sup>a</sup>			
	$\text{TiO}_2$		(CNT- $\text{TiO}_2$ )ox		$\text{TiO}_2$		(CNT- $\text{TiO}_2$ )ox	
	473 K	673 K	473 K	673 K	473 K	673 K	473 K	673 K
Au	0.13	0.45	0.27	0.13	8.4	9.8	9.5	11
Ir	2.2	2.8	2.1	2.2	5.4	4.7	5.0	12
Pd	5.5	0.74	2.7	1.8	6.8	7.6	7.4	8.1
Pt	9.8	1.4	23	1.0	2.6	25	7.2	11

<sup>a</sup> Dimension variation is given as Supplementary Information, Table S11.

in the CNT phase, not only at the external surface of the nanotubes, but also in its interior (Fig. 2f inset).

Diffuse reflectance UV-Vis spectra of  $\text{TiO}_2$  and (CNT- $\text{TiO}_2$ )ox materials loaded with different metals reduced at 673 K can be observed in Fig. 3. As expected,  $\text{TiO}_2$  has no absorption above its fundamental absorption sharp edge rising at 400 nm. In the case of the  $\text{TiO}_2$ -based materials (Fig. 3a), the introduction of the metals led to an increase in the absorption in the visible range. For Au- $\text{TiO}_2$ , an absorption band between 450 and 650 nm could be observed, peaking at 580 nm, characteristic of gold surface plasmon resonance [32].

As expected, for (CNT- $\text{TiO}_2$ )ox loaded with the different metals, a further increase in absorption mainly in the visible spectral range is observed due to the introduction of the CNT phase (Fig. 3b). In CNT- $\text{TiO}_2$  composite photocatalysts this increase in the absorption promoted by CNT has been ascribed to both the capacity of the carbon phase to absorb light and also to the creation of an electronic interphase interaction between CNT and  $\text{TiO}_2$  phases [14,33,34].

### 3.2. Photocatalytic hydrogen generation using different CNT- $\text{TiO}_2$ composites

Methanol is generally used as sacrificial electron donor for the screening of catalysts for  $\text{H}_2$  production by photocatalytic reforming. Methanol possesses interesting properties for this type of processes namely a simple molecular structure, high H:C ratio and the possibility to be obtained from biomass-derived sources [35].

In this work Pt/ $\text{TiO}_2$ -473, Pt/CNTox- $\text{TiO}_2$ -473 and Pt/(CNT- $\text{TiO}_2$ )ox-473 were used as photocatalysts for hydrogen production from water/methanol solutions. A reaction with reference  $\text{TiO}_2$  was also performed for comparison purposes, which resulted in the production of a residual amount of  $\text{H}_2$  (Fig. 4). Typical reactions were carried out for 2 h, under near-UV to visible irradiation conditions. The main goal was to assess the effect of the presence of carbon nanotubes and the synthesis procedures of CNT- $\text{TiO}_2$  composites in the overall  $\text{H}_2$  production efficiency.

The use of both neat  $\text{TiO}_2$  and CNT- $\text{TiO}_2$  composite catalysts led to the generation of  $\text{H}_2$  from methanol solutions (Fig. 4). Nomikos et al. have recently reported a kinetic and mechanistic study on  $\text{H}_2$  production from methanol using a Pt/ $\text{TiO}_2$  catalyst under near-UV ( $\lambda = 365 \text{ nm}$ ) irradiation [36]. In that work the authors describe the photocatalytic reforming of methanol starting with the adsorption of methanol on  $\text{TiO}_2$  forming methoxy species, which are progressively oxidized into formaldehyde, dioxymethylene, formate species and ultimately  $\text{CO}_2$ .  $\text{H}_2$  is generated from the protons released during the oxidation of such species, which are reduced by photogenerated electrons at the surface of the metal cocatalyst nanoparticles.

The rate of  $\text{H}_2$  evolution increased in the first 30 min of reaction, reaching then a plateau (Fig. 4a). It is clear that the composite materials promote an increase in the efficiency of the photocatalytic process when compared with neat  $\text{TiO}_2$ . A 53% increase in the amount of  $\text{H}_2$  generated after 2 h of irradiation was achieved when CNTox- $\text{TiO}_2$  was used as catalyst. Moreover, for the (CNT- $\text{TiO}_2$ )ox material, this increase in  $\text{H}_2$  generation rate was even more pronounced. After 2 h of irradiation, a total of 485  $\mu\text{mol}$  of  $\text{H}_2$  was generated using this photocatalyst, contrasting with 205  $\mu\text{mol}$  produced using Pt/ $\text{TiO}_2$ -473 (Fig. 4b).

The above results show that the preparation method has a significant influence on the efficiency of the CNT- $\text{TiO}_2$  catalysts. The higher surface area of the composite materials when compared to bare  $\text{TiO}_2$  may play a role in the enhanced efficiency of the CNT- $\text{TiO}_2$  catalysts, since the later possess a higher availability of active sites for adsorption and reaction. A figure of merit for evaluating the overall efficiency of catalysts is to compare the reaction rate per unit surface area ( $r/S_{\text{BET}}$ , Table 1). By evaluation of this parameter,



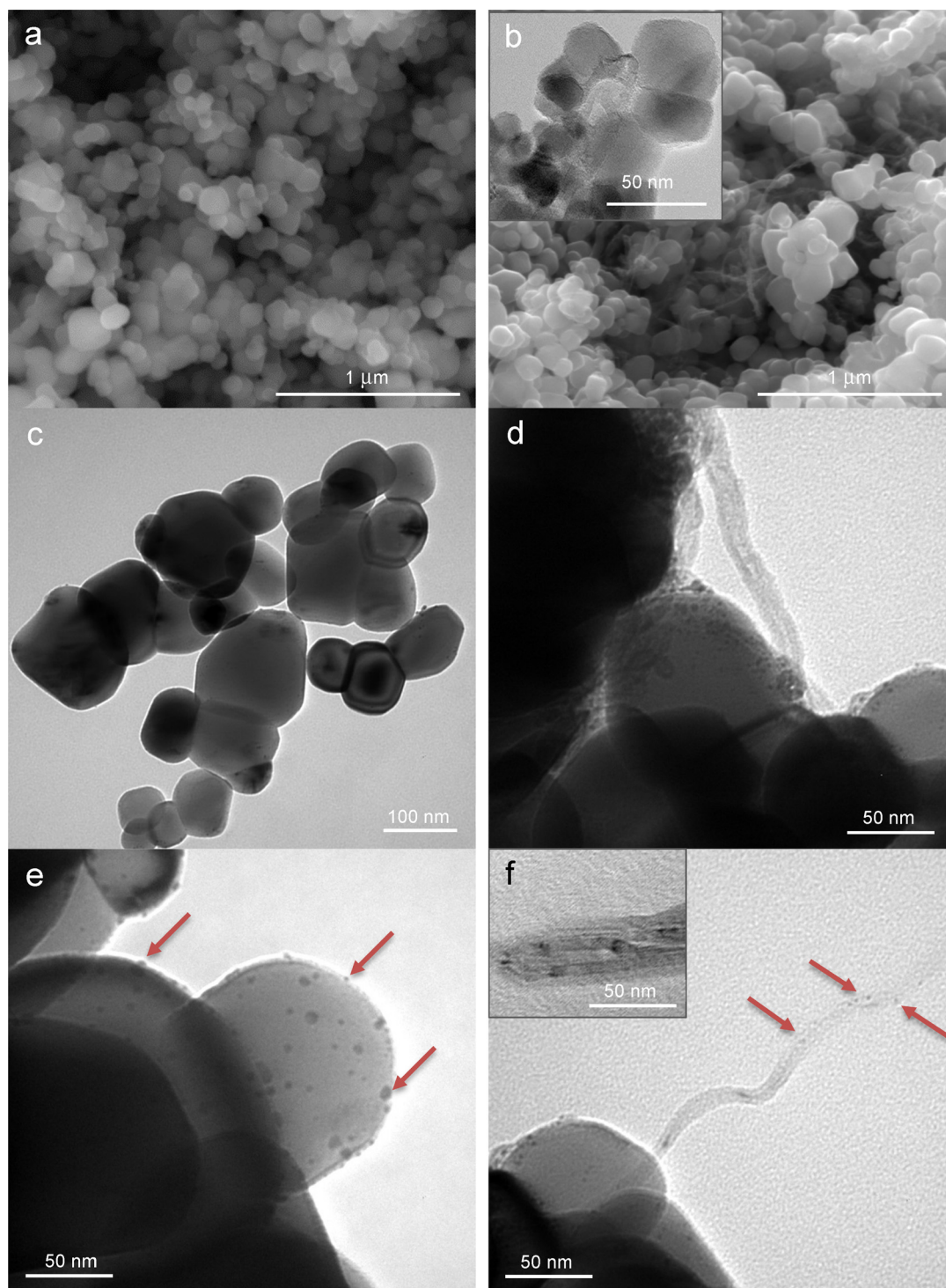


**Fig. 2.** SEM micrographs of  $\text{TiO}_2$  (a) and  $(\text{CNT-TiO}_2)\text{ox}$  (b); TEM images of  $\text{Pt/TiO}_2$ -473 (c and e) and  $\text{Pt}/(\text{CNT-TiO}_2)\text{ox}$ -473 (d and f). Inset of (b): HRTEM image of  $\text{Pt}/(\text{CNT-TiO}_2)\text{ox}$ . Arrows in (e) and (f) are pointing to Pt nanoparticles.

it can be stated that  $\text{Pt/TiO}_2$ -473 shows the highest efficiency followed by  $\text{Pt/CNTox-TiO}_2$ -473 and finally by  $\text{Pt}/(\text{CNT-TiO}_2)\text{ox}$ -473, which follows an inverse order when comparing  $r$  values (Table 1). These results indicate that the surface area cannot be the only factor accounting for the efficiency of the photocatalysts.

The better performance shown by the catalyst prepared with  $(\text{CNT-TiO}_2)\text{ox}$  may be related to the stronger interphase interaction between  $\text{TiO}_2$  and CNT phases, promoted by the oxidative treatment, as previously demonstrated by ATR analysis. The one-pot CNT

functionalization and  $\text{CNT-TiO}_2$  synthesis may promote chemical bonding between both phases, which would drive to more efficient electron transfer upon photoexcitation.

### 3.3. Effect of the nature and reduction temperature of the cocatalyst

The presence of a metal cocatalyst is for most semiconductor photocatalysts a *sine qua non* condition in efficient  $\text{H}_2$  generation

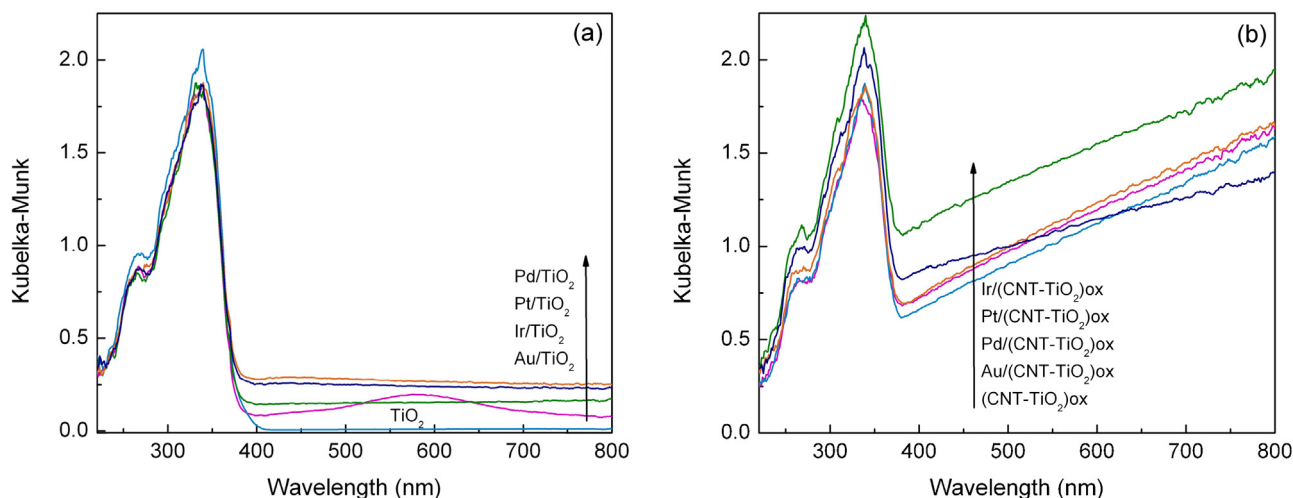


Fig. 3. Diffuse reflectance UV–Vis spectra of  $\text{TiO}_2$  (a) and  $(\text{CNT-TiO}_2)_{\text{ox}}$  (b) based materials calcined and reduced at 473 K.

even in the presence of sacrificial electron donors. This is normally due to the facile recombination of electron-hole pairs before charge migration to the surface of the semiconductor, as well as to the slow consumption of these charges in surface reactions [37]. Noble metals are normally used as cocatalysts, whose functions consist on trapping electrons and providing effective proton reduction sites to form  $\text{H}_2$ . The electron capturing ability is largely determined by the work function of the noble metal, which should be greater than that of the semiconductor. Among the various noble metals, Pt possesses the larger work function, *i.e.* higher ability to trap electrons, justifying the use of this metal as cocatalyst in most of the photocatalytic studies for  $\text{H}_2$  generation [38]. Nevertheless, the synthesis conditions of metal-loaded semiconductors are known to greatly affect several structural properties such as metal dispersion and particle size.

In the present work,  $\text{TiO}_2$  and  $(\text{CNT-TiO}_2)_{\text{ox}}$  were loaded with different noble metals namely Pt, Pd, Au and Ir by traditional incipient wetness impregnation followed by a thermal treatment consisting in a calcination and a reduction step. Materials were heat-treated at two different temperatures: 473 and 673 K.

The rates of  $\text{H}_2$  production ( $r$ ) from water/methanol solutions when the production of gas stabilized are listed in Table 2. Regarding metal-loaded  $\text{TiO}_2$  materials, an increase in the

efficiency of  $\text{H}_2$  generation using Au and Ir catalysts treated at 673 K was observed, when comparing to those calcined and reduced at 473 K, which may be related to the higher reduction temperatures of both metals, as disclosed in the TPR profiles. This enhancement in the photocatalytic activity was of 27% for Ir- $\text{TiO}_2$ , while a 3.3 fold increase in  $r$  was observed for Au- $\text{TiO}_2$ . In the case of Pd- and Pt-loaded  $\text{TiO}_2$ , a detrimental effect was observed by increasing the reduction temperature, which may be attributed to metal particle sintering, as confirmed by the increase in the dimensions of the metal nanoparticles ( $d_M$ ) determined by TEM, especially in the case of Pt- $\text{TiO}_2$  (Table 2). For Pd/ $\text{TiO}_2$  the loss of activity can also be attributed to a strong metal support interaction (SMSI) effect, as previously reported in the literature for this type of catalyst [39–41]. Sá et al. have reported the occurrence of reduced titanium oxide layers over palladium (SMSI state) for reduction temperatures above 623 K [39].

Metal loaded- $(\text{CNT-TiO}_2)_{\text{ox}}$  materials treated at 673 K were in general less active than those obtained at 473 K, which can be related to the increase in the dimensions of the metal particles as well as to the existence of detrimental metal-support interactions as previously described for Pd/ $\text{TiO}_2$  catalyst reduced at 673 K.

Comparing  $\text{TiO}_2$ - and  $(\text{CNT-TiO}_2)_{\text{ox}}$ -based catalysts, a notorious increase (2.4 fold) in  $r$  was obtained for the Pt-loaded materials

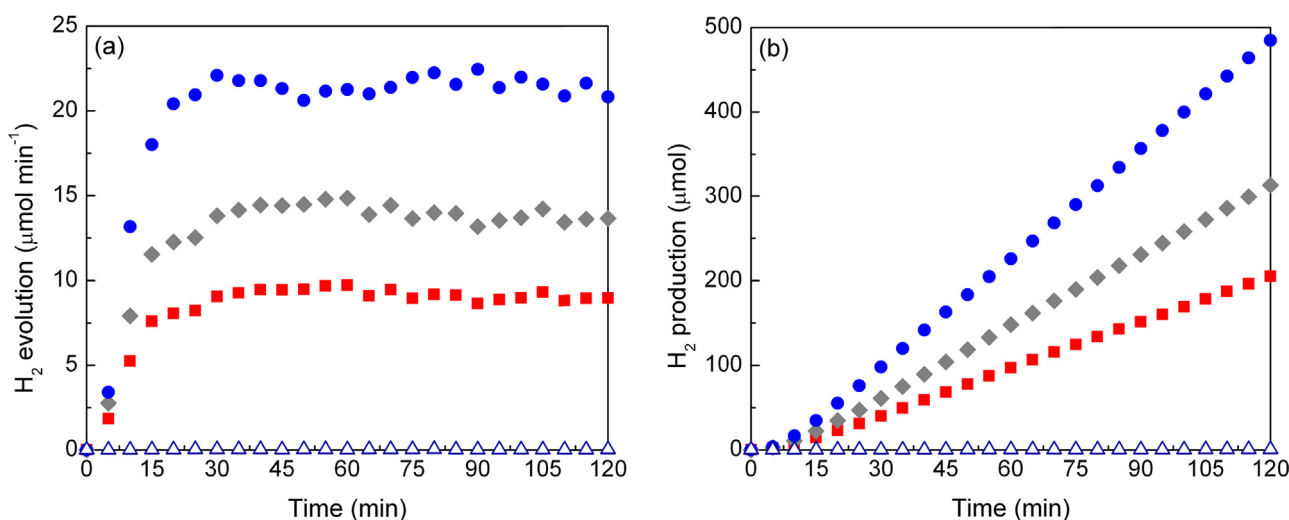
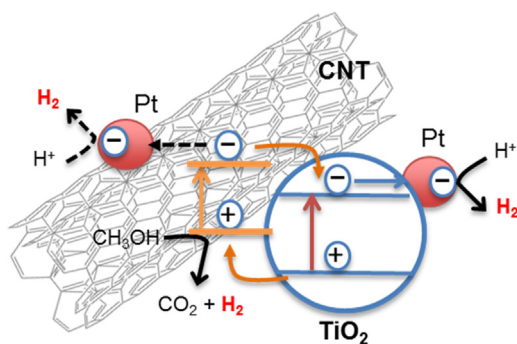


Fig. 4. Rate of  $\text{H}_2$  evolution (a) and total  $\text{H}_2$  production (b) using bare  $\text{TiO}_2$  ( $\Delta$ ), Pt/ $\text{TiO}_2$ -473 ( $\blacksquare$ ), Pt/CNTox- $\text{TiO}_2$ -473 ( $\blacklozenge$ ) and Pt/ $(\text{CNT-TiO}_2)_{\text{ox}}$ -473 ( $\bullet$ ) from 10 vol.% methanol solutions.



**Fig. 5.** Schematic representation of the photocatalytic mechanism of  $H_2$  generation from water/methanol solutions under near UV to visible light irradiation using Pt/(CNT-TiO<sub>2</sub>)<sub>ox</sub>-473 catalyst.

treated at 473 K. For the remaining materials treated at this temperature, dissimilar effects promoted by the presence of CNT were observed: a positive effect was obtained for Au-loaded catalyst (48% increase in  $r$ ); practically no effect was observed for Ir catalysts; and a detrimental effect was obtained using Pd/(CNT-TiO<sub>2</sub>)<sub>ox</sub>-473 (50% decrease in  $r$ ) when comparing with the respective TiO<sub>2</sub> catalyst.

Among all the synthesized materials, Pt/(CNT-TiO<sub>2</sub>)<sub>ox</sub>-473 revealed to be the most efficient photocatalyst for  $H_2$  generation from water/methanol solutions. Several factors may be related to the enhanced performance of this catalyst, namely the higher work function of Pt when compared to that of Ir, Pd and Au, the lower Pt particle dimensions and the synergic effect between TiO<sub>2</sub> and CNT phases.

Bare TiO<sub>2</sub> has a large overpotential for the evolution of  $H_2$  (electrons in the conduction band are above the  $H^+/H_2$  potential only by 0.1–0.2 eV), which results in its practically inactiveness for  $H_2$  generation. Noble metal loading generally results in enhanced  $H_2$  evolution since these metals have low hydrogen overpotential. Moreover, the work functions of the noble metals used in this study ( $\Phi_{Pt} = 5.65$  eV >  $\Phi_{Pd} = 5.55$  eV >  $\Phi_{Ir} = 5.27$  eV >  $\Phi_{Au} = 5.10$  eV) are larger than that of TiO<sub>2</sub> (4.2 eV) making possible the formation of a Schottky barrier with the consequent decrease in the recombination of electrons and holes and increasing the lifetime of the charge separation state [37,42]. The larger the work function of the loaded metal, the stronger the Schottky barrier effect, which is in accordance with the best photocatalytic activity of the Pt-loaded catalysts, followed by Pd-, Ir- and Au- containing materials.

The role played by CNTs in CNT-TiO<sub>2</sub> composite catalysts has been discussed in previous works using similar materials. The CNT may work as dispersing media for the TiO<sub>2</sub> particles, or as photosensitizer [14,17,34,43]. Characterization confirmed the first effect, as an increase in the  $S_{BET}$  of the composite materials was observed when compared to bare TiO<sub>2</sub>. Nevertheless, as previously discussed taking into consideration  $r/S_{BET}$  quantification, the higher surface area cannot be considered as the main feature of CNT-TiO<sub>2</sub> composite materials.

It is then more reasonable to ascribe the synergy effect to the action of CNT as a photosensitizer. In the present work, since the irradiation source used emits at  $\lambda \geq 365$  nm, it is expected that both TiO<sub>2</sub> and CNT could be photo-excited. Electrons from the valence band of TiO<sub>2</sub> are excited to the conduction band of the semiconductor and transferred to Pt nanoparticles reducing protons and generating  $H_2$ . On the other hand, positively charged holes may migrate to the CNT phase to oxidize methanol, as shown in Fig. 5.

At the same time, due to the strong interphase interaction between CNT and TiO<sub>2</sub>, photo-excited electrons in the CNT phase may migrate to the conduction band of TiO<sub>2</sub>, increasing the

availability of these species in the TiO<sub>2</sub> phase and therefore enhancing  $H_2$  production. Since Pt particles could be also found in CNT, as can be observed in Fig. 2f, electrons may also migrate to those particles, which act as active sites for  $H_2$  generation.

### 3.4. Photocatalytic hydrogen generation from saccharides

Pt/TiO<sub>2</sub>-473 and Pt/(CNT-TiO<sub>2</sub>)<sub>ox</sub>-473 were used for  $H_2$  generation from 0.02 M aqueous solutions of four different saccharides: arabinose (C<sub>5</sub>H<sub>10</sub>O<sub>5</sub>), fructose (C<sub>6</sub>H<sub>12</sub>O<sub>6</sub>), glucose (C<sub>6</sub>H<sub>12</sub>O<sub>6</sub>), and cellobiose (C<sub>12</sub>H<sub>22</sub>O<sub>11</sub>). The choice of such compounds was driven by the intention of searching for a relationship between their capacity of generating  $H_2$  and their intrinsic properties such as structural complexity and H:C molar ratio [21,44]. The  $H_2$  evolution profiles obtained from the photocatalytic reforming of the different saccharides using the two selected catalysts are shown in Fig. 6 and the amounts of  $H_2$  generated at the end of 2 h of irradiation are summarized in Table 3.

As can be observed in Fig. 6, the profiles of  $H_2$  evolution from saccharides were different than those observed for the reactions using methanol as sacrificial reagent (Fig. 4a), where a steady state was observed at the end of 30 min of irradiation. In the case of the reactions with saccharides, the amount of  $H_2$  generated increases in the first 15 to 30 min of irradiation and then gradually declines. This behavior may be attributed to the lower sacrificial reagent concentration (0.02 M contrasting with 2.5 M in the case of methanol) and its faster depletion, to the lower C:H ratio and also to the higher complexity of the molecular structure and of the mechanism involved in the degradation of saccharides when compared to that of methanol [36,45]. Nevertheless, for the reactions using Pt/(CNT-TiO<sub>2</sub>)<sub>ox</sub>-473, this depletion on the rate of  $H_2$  generation was not so abrupt as in the case of Pt/TiO<sub>2</sub>-473, which confirms the different mechanisms occurring after photoexcitation.

Regarding the results obtained with Pt/TiO<sub>2</sub>-473 catalyst, the amounts of  $H_2$  generation varied following the order arabinose > glucose > fructose > cellobiose, which seems to be related with the progressively increasing complexity of the carbon skeleton [21,46], rather than with the stoichiometric H:C ratio on each molecule. HPLC analysis of the liquid phase at the end of the photocatalytic reactions using Pt/TiO<sub>2</sub>-473 revealed that arabinose conversion was the highest among the saccharides studied. At the end of 2 h of irradiation 9.6% of the starting compound was degraded. The concentration of the initial compound decreased nearly 4.0% in the case of fructose and glucose and 5.6% for the reaction with cellobiose. A molar ratio ( $m$ ) between the quantity of  $H_2$  generated and the amount of saccharide consumed was determined and listed in Table 3. For the reactions using Pt/TiO<sub>2</sub>-473, the lowest  $m$  value was obtained for cellobiose, followed by glucose, arabinose and finally fructose. These findings reveal that apart from the structural complexity and H:C stoichiometry, other factors must account for the efficiency of photocatalytic  $H_2$  production from saccharides. Bahruji et al. found that in the case of photocatalytic reforming of alcohols using Pd/TiO<sub>2</sub> catalysts, the main characteristic that determines their reactivity is the availability of hydrogen atoms in the  $\alpha$ -position with respect to the OH group and the ease of dissociation of the  $\alpha$ -C–C bond [7]. This can be a rationalization for the  $m$  values resulting from the reactions using Pt/TiO<sub>2</sub> catalyst, since fructose and arabinose have the highest number of  $\alpha$ -hydrogens, followed by glucose and cellobiose.

Comparing the efficiency of the two catalysts it could be stated that Pt/(CNT-TiO<sub>2</sub>)<sub>ox</sub>-473 show better  $H_2$  production performance than Pt/TiO<sub>2</sub>-473, except for the reaction with arabinose. In that case, a 14% decrease in the amount of  $H_2$  generation was obtained when comparing TiO<sub>2</sub> and (CNT-TiO<sub>2</sub>)<sub>ox</sub> catalysts. In contrast, the most evident result was obtained in the presence of cellobiose, with a 2.8 fold increase in the amount of

**Table 3**H<sub>2</sub> generated from saccharides (0.02 M) at 2 h of irradiation using Pt/TiO<sub>2</sub>-473 and Pt/(CNT-TiO<sub>2</sub>)<sub>ox</sub>-473 catalysts.

Saccharide	Pt/TiO <sub>2</sub> -473			Pt/(CNT-TiO <sub>2</sub> ) <sub>ox</sub> -473		
	H <sub>2</sub> (μmol)	X <sub>Saccharide</sub> (%)	m <sup>a</sup>	H <sub>2</sub> (μmol)	X <sub>Saccharide</sub> (%)	m <sup>a</sup>
Arabinose	35.7	9.61	0.109	30.6	7.72	0.116
Fructose	11.9	3.92	0.195	17.5	2.10	0.245
Glucose	24.4	3.67	0.0890	33.7	3.15	0.301
Cellobiose	9.59	5.60	0.0503	26.8	3.90	0.202

<sup>a</sup> m: mol of H<sub>2</sub> generated per mol of saccharide converted.

the H<sub>2</sub> generated at the end of 2 h of irradiation. In the case of the reactions with glucose and fructose solutions, this increase was 38 and 47%, respectively. Although the use of Pt/(CNT-TiO<sub>2</sub>)<sub>ox</sub>-473 catalyst originated in general higher amounts of H<sub>2</sub>, saccharide conversion was lower but the values of *m* higher than the observed for the reactions using Pt/TiO<sub>2</sub>-473 catalyst (Table 3), which may be rationalized by the existence of distinct mechanisms involved in the H<sub>2</sub> production. It has been reported that the initial step of photocatalytic reforming of saccharides using Pt/TiO<sub>2</sub> catalysts consists in the coordination of OH groups to under-coordinated Ti<sup>IV</sup> surface sites [46]. Subsequently, H<sup>+</sup> and alkoxide anions are formed. While the former may be reduced by photogenerated electrons at the surface of Pt particles to yield H<sub>2</sub>, the later react with

photogenerated holes resulting in the formation of radical species. Those species attack saccharide molecules originating aldehydes and carboxylic acid derivatives, which undergo several deprotonation/decarboxylation cycles until they are ultimately converted to CO<sub>2</sub> [38,46]. In the case of Pt/(CNT-TiO<sub>2</sub>)<sub>ox</sub>-473, due to the different photoactivation mechanism, it is expected that a higher availability of electrons at the Pt particles occur (Fig. 5) leading to an increase in the contribution of the water-proton reduction in the total amount of H<sub>2</sub> generated during the photocatalytic reforming reactions. Moreover, a 4-fold increase in *m* was observed for the photocatalytic reactions with cellobiose using the composite catalyst in comparison with Pt/TiO<sub>2</sub>-473, while it kept practically constant when arabinose was used as sacrificial electron donor.

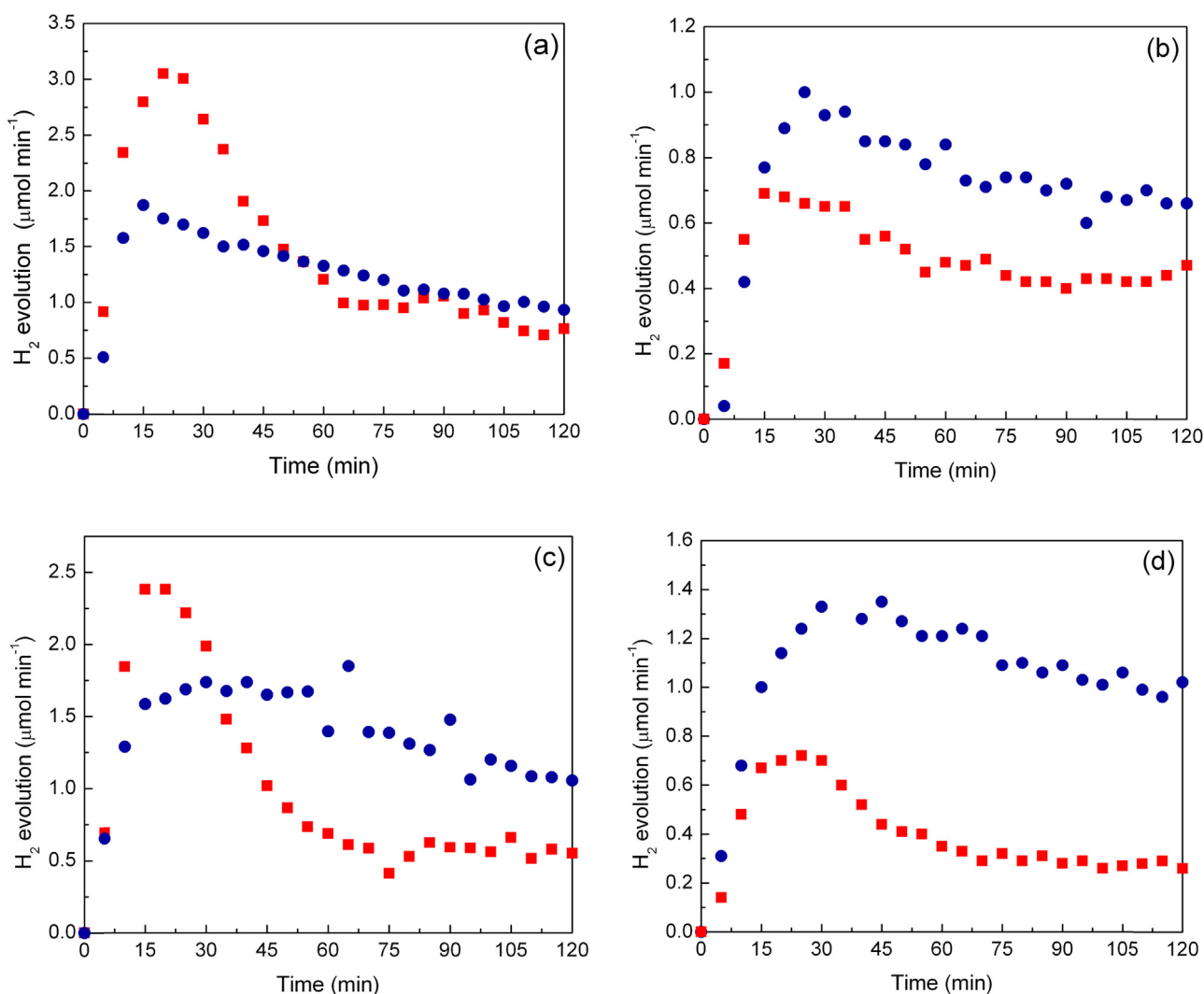


**Fig. 6.** H<sub>2</sub> evolution profiles during the photocatalytic reactions using Pt/TiO<sub>2</sub>-473 (■) and Pt/(CNT-TiO<sub>2</sub>)<sub>ox</sub>-473 (●) from 0.02 M solutions of arabinose (a), fructose (b), glucose (c) and cellobiose (d).



These results suggest that Pt/(CNT-TiO<sub>2</sub>)<sub>ox</sub>-463 is more efficient for the photocatalytic reforming of saccharides presenting more complex molecular structures, such as cellobiose, rather than for smaller molecules, like arabinose. This may be related to the higher surface area of the composite material, reducing diffusional limitations particularly in the case of larger molecules, and also to the higher number of active sites available for reaction.

#### 4. Conclusions

CNT-TiO<sub>2</sub> catalysts were efficiently used for H<sub>2</sub> generation by photocatalytic reforming of biomass-derived compounds. The efficiency of such catalysts was related with the composite synthesis procedure. A one-pot route combining CNT oxidation and composite synthesis resulted in the formation of materials with enhanced photocatalytic activity, which was attributed to the creation of a stronger interphase interaction between CNT and TiO<sub>2</sub>.

Nanoparticles of Pt, Au, Ir and Pd were introduced in TiO<sub>2</sub> and (CNT-TiO<sub>2</sub>)<sub>ox</sub> by an incipient wetness method. Compared to the non-loaded catalysts, noble-metal loading promotes the photocatalytic production of H<sub>2</sub> from methanol- and saccharide-containing solutions. This is due to the lower overpotential for H<sub>2</sub> evolution on the metal loaded photocatalysts when compared to the bare catalysts. The relative efficiency of the noble metals for H<sub>2</sub> production can be related to the work function of each co-catalyst and to the synthesis conditions namely the calcination/reduction temperature. In general, materials treated at 473 K show increased efficiency than those obtained at 673 K, mostly due to metal particle sintering and strong metal support interaction.

Pt/(CNT-TiO<sub>2</sub>)<sub>ox</sub>-473 was the most active catalyst for H<sub>2</sub> generation from water/methanol solutions producing a 2.4 increase in the rate of H<sub>2</sub> evolution when compared to Pt/TiO<sub>2</sub>-473. This synergic effect is attributed to an increase in the efficiency of charge separation and mobility in the composite material.

Saccharides are good candidates as sacrificial electron donors for photocatalytic hydrogen generation. The efficiency for H<sub>2</sub> generation using Pt/TiO<sub>2</sub>-473 increases with the decreasing complexity of the molecular structure of the saccharide. In the case of the reactions using Pt/(CNT-TiO<sub>2</sub>)<sub>ox</sub>-473, the superior amounts of H<sub>2</sub> generated from fructose, glucose and cellobiose solutions is attributed to an increase of the contribution of the water-proton reduction at the surface of the noble metal particles.

#### Acknowledgments

This work was supported by Project PEst-C/EQB/LA0020/2013 and PEst-OE/QUI/UI0616/2014, financed by FEDER through COMPETE–Programa Operacional Factores de Competitividade, and by FCT–Fundação para a Ciência e a Tecnologia, and co-financed by QREN, ON2 and FEDER through Projects NORTE-07-0124-FEDER-000015 and NORTE-07-0162-FEDER-000050. FCT is acknowledged for funding the Doctoral grant SFRH/BD/79878/2011 (MJS). AMTS acknowledges the FCT Investigator 2013 Programme (IF/01501/2013), with financing from the European Social Fund and the Human Potential Operational Programme.

We are indebted to Dr. Carlos Sá and the CEMUP team for technical assistance and advice with SEM/EDXS measurements.

#### Appendix A. Supplementary data

Supplementary data associated with this article can be found, in the online version, at <http://dx.doi.org/10.1016/j.apcatb.2014.10.032>.

#### References

- [1] C. Acar, I. Dincer, *Int. J. Hydrogen Energy* 39 (2014) 1–12.
- [2] E. Cetinkaya, I. Dincer, G.F. Naterer, *Int. J. Hydrogen Energy* 37 (2012) 2071–2080.
- [3] I. Dincer, *Int. J. Hydrogen Energy* 37 (2012) 1954–1971.
- [4] J.D. Holladay, J. Hu, D.L. King, Y. Wang, *Catal. Today* 139 (2009) 244–260.
- [5] M. Ni, D.Y.C. Leung, M.K.H. Leung, *Int. J. Hydrogen Energy* 32 (2007) 3238–3247.
- [6] N. Armaroli, V. Balzani, *ChemSusChem* 4 (2011) 21–36.
- [7] H. Bahruji, M. Bowker, P.R. Davies, L.S. Al-Mazroai, A. Dickinson, J. Greaves, D. James, L. Millard, F. Pedrono, J. Photochem. Photobiol., A 216 (2010) 115–118.
- [8] D.I. Kondarides, V.M. Daskalaki, A. Patsoura, X.E. Verykios, *Catal. Lett.* 122 (2008) 26–32.
- [9] M. Ilie, B. Cojocaru, V.J. Parvulescu, H. Garcia, *Int. J. Hydrogen Energy* 36 (2011) 15509–15518.
- [10] A. Speltini, M. Sturini, D. Dondi, E. Annovazzi, F. Maraschi, V. Caratto, A. Profumo, A. Buttafava, *Photochem. Photobiol. Sci.* 13 (2014) 1410–1419.
- [11] A. Speltini, M. Sturini, F. Maraschi, D. Dondi, A. Serra, A. Profumo, A. Buttafava, A. Albini, *Int. J. Hydrogen Energy* 39 (2014) 11433–11440.
- [12] R. Leary, A. Westwood, *Carbon* 49 (2011) 741–772.
- [13] K. Woan, G. Pyrgiotakis, W. Sigmund, *Adv. Mater.* 21 (2009) 2233–2239.
- [14] C.G. Silva, J.L. Faria, *Appl. Catal., B* 101 (2010) 81–89.
- [15] L.M. Pastrana-Martínez, S. Morales-Torres, S.K. Papageorgiou, F.K. Katsaros, G.E. Romanos, J.L. Figueiredo, J.L. Faria, P. Falaras, A.M.T. Silva, *Appl. Catal., B* 142–143 (2013) 101–111.
- [16] B. Ahmmad, Y. Kusumoto, S. Somekawa, M. Ikeda, *Catal. Commun.* 9 (2008) 1410–1413.
- [17] K. Dai, T. Peng, D. Ke, B. Wei, *Nanotechnology* 20 (2009) 124603.
- [18] K. Dai, X. Zhang, K. Fan, P. Zeng, T. Peng, *J. Nanomater.* 2014 (2014) 694073.
- [19] G. Khan, S.K. Choi, S. Kim, S.K. Lim, J.S. Jang, H. Park, *Appl. Catal., B* 142–143 (2013) 647–653.
- [20] Y.K. Kim, H. Park, *Appl. Catal., B* 125 (2012) 530–537.
- [21] X. Fu, J. Long, X. Wang, D.Y.C. Leung, Z. Ding, L. Wu, Z. Zhang, Z. Li, X. Fu, *Int. J. Hydrogen Energy* 33 (2008) 6484–6491.
- [22] D.I. Kondarides, A. Patsoura, X.E. Verykios, *J. Adv. Oxid. Technol.* 13 (2010) 116–123.
- [23] I.D. Rosca, F. Watari, M. Uo, T. Akasaka, *Carbon* 43 (2005) 3124–3131.
- [24] A. Speltini, D. Merli, E. Quartarone, A. Profumo, *J. Chromatogr. A* 1217 (2010) 2918–2924.
- [25] R.R.N. Marques, M.J. Sampaio, P.M. Carrapiço, C.G. Silva, S. Morales-Torres, G. Dražić, J.L. Faria, A.M.T. Silva, *Catal. Today* 209 (2013) 108–115.
- [26] E.G. Rodrigues, S.A.C. Carabineiro, J.J. Delgado, X. Chen, M.F.R. Pereira, J.J.M. Órfão, *J. Catal.* 285 (2012) 83–91.
- [27] J.L. Figueiredo, M.F.R. Pereira, M.M.A. Freitas, J.J.M. Órfão, *Carbon* 37 (1999) 1379–1389.
- [28] J.L. Figueiredo, M.F.R. Pereira, M.M.A. Freitas, J.J.M. Órfão, *Ind. Eng. Chem. Res.* 46 (2007) 4110–4115.
- [29] J. Chen, Q. Chen, Q. Ma, *J. Colloid Interface Sci.* 370 (2012) 32–38.
- [30] C. Moreno-Castilla, M.V. López-Ramón, F. Carrasco-Marín, *Carbon* 38 (2000) 1995–2001.
- [31] M. Monthieux, B.W. Smith, B. Burteaux, A. Claye, J.E. Fischer, D.E. Luzzi, *Carbon* 39 (2001) 1251–1272.
- [32] C.G. Silva, R. Juárez, T. Marino, R. Molinari, H. García, *J. Am. Chem. Soc.* 133 (2011) 595–602.
- [33] B. Gao, G.Z. Chen, G. Li Puma, *Appl. Catal., B* 89 (2009) 503–509.
- [34] W. Wang, P. Serp, P. Kalck, J.L. Faria, *Appl. Catal., B* 56 (2005) 305–312.
- [35] G. Wu, T. Chen, W. Su, G. Zhou, X. Zong, Z. Lei, C. Li, *Int. J. Hydrogen Energy* 33 (2008) 1243–1251.
- [36] G.N. Nomikos, P. Panagiotopoulou, D.I. Kondarides, X.E. Verykios, *Appl. Catal., B* 146 (2014) 249–257.
- [37] J. Yang, D. Wang, H. Han, C. Li, *Acc. Chem. Res.* 46 (2013) 1900–1909.
- [38] K. Shimura, H. Yoshida, *Energy Environ. Sci.* 4 (2011) 2467–2481.
- [39] J. Sá, J. Bernardi, J. Anderson, *Catal. Lett.* 114 (2007) 91–95.
- [40] S.J. Tauster, S.C. Fung, *J. Catal.* 55 (1978) 29–35.
- [41] S.J. Tauster, S.C. Fung, R.L. Garten, *J. Am. Chem. Soc.* 100 (1978) 170–175.
- [42] D.E. Eastman, *Phys. Rev. B* 2 (1970) 1–2.
- [43] Y. Ou, J. Lin, S. Fang, D. Liao, *Chem. Phys. Lett.* 429 (2006) 199–203.
- [44] A. Patsoura, D.I. Kondarides, X.E. Verykios, *Catal. Today* 124 (2007) 94–102.
- [45] G.L. Chiarello, M.H. Aguirre, E. Selli, *J. Catal.* 273 (2010) 182–190.
- [46] M. Cargnello, A. Gasparotto, V. Gombac, T. Montini, D. Barreca, P. Fornasiero, *Eur. J. Inorg. Chem.* 2011 (2011) 4309–4323.